

Article

Simple and Robust MPPT Current Control of a Wound Rotor Synchronous Wind Generator

Lucky Dube , Graham C. Garner , Karen S. Garner  and Maarten J. Kamper 

Department of Electrical and Electronic Engineering, Stellenbosch University, Stellenbosch 7600, South Africa

* Correspondence: kamper@sun.ac.za

Abstract: In the search for efficient non-permanent magnet variable-speed wind generator solutions, this paper proposes a maximum power point tracking (MPPT) current-control method for a wound rotor synchronous wind generator. The focus is on direct-drive, medium-speed wind generators. In the proposed method, the currents of the wound rotor synchronous generator (WRSG) are optimally adjusted according to the generator speed to ensure maximum power generation from the wind turbine without needing information on wind speed. The design, modeling, and simulation of the MPPT current controllers are done in Matlab/Simulink with the WRSG in the synchronous reference frame. The controller is put to the test using different wind speed profiles between cut-in and rated speeds. The simulation results indicate that the proposed current control method is simple, effective, and robust, suggesting its practical implementation. To validate the simulation results, experimental work on a 4.2 kW WRSG prototype system is presented to demonstrate the stability and robustness of the MPPT current control method in operating the turbine at or near the maximum power point.

Keywords: current control; maximum power point tracking (MPPT); synchronous wind generator; wound rotor



Citation: Dube, L.; Garner, G.C.; Garner, K.S.; Kamper, M.J. Simple and Robust MPPT Current Control of a Wound Rotor Synchronous Wind Generator. *Energies* **2023**, *16*, 3290. <https://doi.org/10.3390/en16073290>

Academic Editor: Adrian Ilinca

Received: 7 March 2023

Revised: 30 March 2023

Accepted: 3 April 2023

Published: 6 April 2023



Copyright: © 2023 by the authors. Licensee MDPI, Basel, Switzerland. This article is an open access article distributed under the terms and conditions of the Creative Commons Attribution (CC BY) license (<https://creativecommons.org/licenses/by/4.0/>).

1. Introduction

As a solution to the effects of global warming caused by the extensive use of fossil fuels to generate electricity, the world is shifting its focus to renewable energy sources, such as hydro, wind, solar, biomass, geothermal, and tidal. Hydropower remains the most widely used type of modern renewable energy source worldwide, but the wind energy sector is expanding rapidly [1]. Wind generators are important parts of wind turbine systems to capture wind energy because they transform the mechanical power of the rotor blades into electrical power. In the wind energy industry, the most prominent generator technologies are the permanent magnet synchronous generator (PMSG), electrically excited synchronous generator (EESG), doubly-fed induction generator (DFIG), and the squirrel cage induction generator (SCIG) [2]. Wind generator technologies that use a non-overlapping winding structure have become attractive because they offer advantages such as requiring less copper, cheaper manufacturing costs, reduced torque ripple, and higher torque density [3] compared to a traditional overlapping winding structure. Recent research studies show that permanent magnet (PM) generators with non-overlapping windings are an important part of the modern wind energy industry because they are very efficient, have a high power factor, and are compact. However, research on competitive rare-earth (RE) free-element wind generators is still important because of how volatile the market is for RE PMs and how sensitive they are to geopolitics (most of the supply chain is in China).

The SCIG and DFIG are non-PM generators used in wind turbine systems due to their mature technology, their simple and robust structure, as well as their economy of maintenance [4]. Their application in wind turbines is disadvantaged because they are rarely built with a high number of pole pairs and, hence, require three-stage gearboxes. Other non-PM generator solutions for wind energy systems include wound rotor synchronous generators

(WRSGs), such as an EESG. Reluctance synchronous generators (RSGs) are also emerging as attractive non-PM wind generator solutions [5]. The WRSG and RSG, such as the PMSG, can be built with a large number of poles and still achieve high efficiency. However, due to their inherent design, RSGs have a poor power factor and hence require relatively high-rated and expensive power converters [6], which makes them rarely used in wind turbines. On the other hand, WRSGs offer excitation windings on the rotor, which provide a controlled excitation flux. As a result of this ability, the WRSG can achieve a near-unity power factor [7], demonstrating its capabilities in wind turbines. In addition, the flux variation capability of WRSG makes it an attractive application for variable-speed wind generation systems because the rotor field current can be varied for maximum power point tracking (MPPT). In the modern wind industry, variable-speed wind turbines are dominant, and their control design for MPPT is very important for extracting maximum power from the wind, and hence maximizing the efficiency of the wind turbine.

In the literature, the fundamental MPPT operation for wind turbine systems that delivers maximum efficiency is primarily comprised of a number of MPPT search techniques that attempt to find the maximum operating point (MPP). The MPPT search methods typically fall into two categories, i.e., direct power control (DPC), which controls the electrical output power of the wind turbine by obtaining the most mechanical power from the wind, and indirect power control (IPC), which directly maximizes the output electrical power of the wind turbine [8]. The IPC includes control techniques, such as tip-speed ratio (TSR), power signal feedback (PSF), and optimal torque (OT). The DPC includes methods such as perturb and observe (P&O)/hill climb search (HCS) and incremental conductance (INC). The DPC methods are generally used in wind turbine systems due to their simple design and ease of implementation, specifically the P&O MPPT algorithms. It observes the deviation in turbine power and adjusts the turbine speed to keep track of the maximum power point [9]. This method, however, deviates while tracing the optimal power point, especially during a wind gust. The TSR IPC technique adjusts the generator speed by using both wind and turbine speeds to keep the TSR at its optimum while tracking the maximum power point [10]. The benefit of this technology is that the control scheme is simple; however, the requirement for real-time measurements of wind and generator speed increases costs. The other two IPC methods, PSF and OT, do not require real-time wind speed measurements, but relatively precise wind speed parameters based on experiments are needed.

The design of the controller, which sends switching signals to the power converters to make sure that a wind turbine works at MPP [11], is another fundamental part of the MPPT operation of wind turbine systems. Traditionally, PID-type MPPT controllers have always been the most popular type of MPPT controllers because of their simple design and implementation. The major drawback of PID controllers is that they are not the most effective controllers across a wide range of operating conditions [12]. So, they often exhibit poor performance when used with nonlinear systems, such as variable-speed wind turbines. For that reason, researchers have looked at the effectiveness of many MPPT algorithms for wind turbines, such as those based on fuzzy logic control [13,14], artificial neural networks [15], the sensorless MPPT algorithm [16,17], and sliding mode control (SMC) [11,18]. The SMC received the most attention of these methods because of its good dynamic response, simple implementation, and robustness against external disturbances and parameter variations [19]. The SMC uses a discontinuous switching law that ensures that the system's state variables will move toward equilibrium from any starting point [20]. The main problem with SMC is that the discontinuous switching in the control law causes a problem called "chattering", which has some bad effects on the steady-state error.

Sensorless MPPT control for wind turbines is an interesting approach because it eliminates the need for mechanical sensors as well as some wind turbine parameters. An optimal sensorless current vector control method for MPPT in variable-speed wind generation based on an interior permanent-magnet synchronous generator was investigated in [16]. In this wind energy system, MPPT is achieved by determining the optimal stator d - and

q -axis current references using only the generator speed, without the need for a wind speed sensor. The experimental results of this work confirmed the effectiveness of the controller.

The main objective of this study is to investigate a simple and robust MPPT current-control method similar to that of [16], but for a WRSG variable-speed wind turbine system. The main contribution of this paper is to investigate the effectiveness of this MPPT technique when used with WRSG-based wind turbines. This is important because most literature studies are focused on PM- and IG-based wind turbine systems. The proposed controller ensures MPPT by determining appropriate generator field current and generator stator output q -axis current reference values as functions of the turbine speed. The d -axis current reference value is kept at zero because the WRSG generates maximum torque when the d -axis current is zero. The focus of the study was on a small-scale, 4.2 kW, medium-speed (between 100 and 500 r/min), direct-drive WRSG-based wind turbine system. The Matlab/Simulink package was used for the simulation of the MPPT current controller wind turbine drive system, while an in-house-designed Pentium control system running Linux was used for experimental validation.

The remainder of this article is organized as follows: Section 2 provides a detailed description of the wind turbine system configuration. Section 3 presents the design and specifications of the WRSG. In Section 4, the WRSG's dynamic modeling is described along with the technique used to determine its simulation parameters. The MPPT method and the proposed current-controller design for maximum power extraction are presented in Section 5. Moreover, the simulation and practical results are provided in Sections 6 and 7, respectively. Lastly, in Section 8, the conclusions are drawn.

2. Description of Wind Turbine System

2.1. Composition of Wind Turbine System

The schematic diagram of the small-scale variable wind speed turbine investigated in this paper is shown in Figure 1. The wind turbine is directly connected to the shaft of a 16-pole WRSG. The WRSG converts the mechanical power of the wind turbine into the alternating current electrical power, which is then actively rectified to the direct current electrical power via a three-phase power converter. The DC link voltage is used to produce the required excitation voltage for the field windings via a DC–DC converter. The remaining power is supplied to a DC grid and can also be connected to an AC grid converter. At the heart of this research work are the two functions, $F_f(\omega_g)$ and $F_q(\omega_g)$, which output the generator current references, i_f and i_q (i_d is always zero), in a manner that ensures that the WRSG and the wind turbine are always operating at maximum efficiency and power.

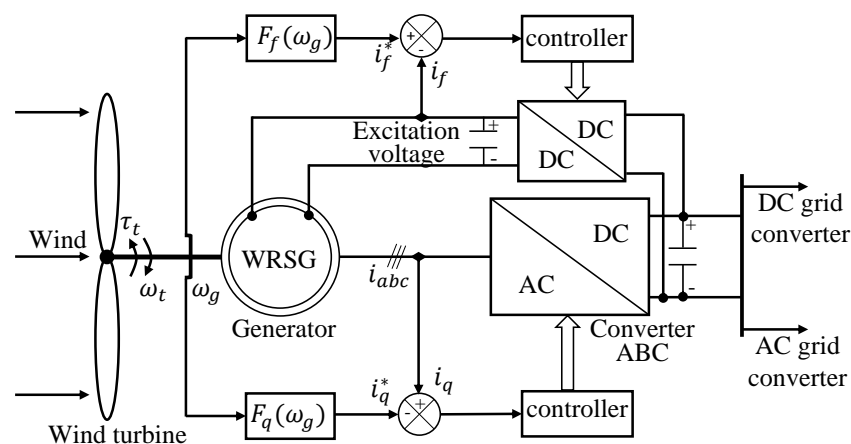


Figure 1. Block diagram of the variable-speed WRSG-based direct-drive wind turbine system.

2.2. Characteristics of the Wind Turbine

The aerodynamic design of the wind turbine determines the amount of power that can be captured from the wind. The available mechanical power of the wind turbine is defined as [18]

$$P_m = \frac{1}{2} \rho A_s v_w^3, \quad (1)$$

where ρ is the air density, kg/m^3 , and v_w is the wind speed, $[\text{m/s}]$. A_s is the sweep area $[\text{m}^2]$ of the wind turbine blades across which a wind stream moves. The amount of power that a wind turbine can capture is practically limited by Betz's law, which states that the maximum theoretical efficiency of the kinetic wind energy that a turbine can capture is 59.3% [21], but modern turbines achieve efficiencies of 45% to 50% [22]. The efficiency is governed by the wind turbine power coefficient, C_p . The C_p of a fixed-pitch wind turbine is given as a function of the tip-speed ratio, Λ , and is defined as

$$\Lambda = \frac{\omega_t R}{v_w}, \quad (2)$$

where ω_t is the turbine speed and R is the radius of the blades. Because the air density ρ and swept area A_s are constant, the maximum turbine power for a certain wind speed occurs at a point where C_p and Λ are maximum [23]. The mechanical turbine power is, therefore, given by

$$P_m = \frac{1}{2} \rho A_s v_w^3 C_p(\Lambda). \quad (3)$$

Figure 2 illustrates the relationship between the turbine power and turbine speed, where the wind speed is a parameter and the MPP curve considered in this study is shown. The cut-in speed at which the turbine starts to rotate and generate power is 100 r/min at a wind speed of 3 m/s. The rated turbine speed is 320 r/min, corresponding to a wind speed of 12 m/s and a generated rated turbine power of 4.2 kW, which corresponds to a rated turbine torque of 126.5 Nm.

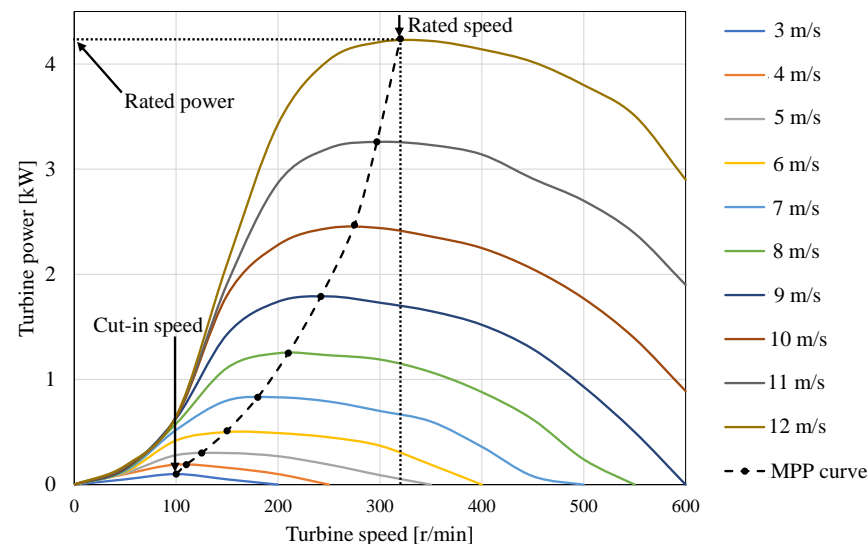


Figure 2. Turbine power versus turbine speed, with the wind speed as a parameter.

3. Design of the WRSG

3.1. WRSG Specifications

The WRSG considered is based on the rated speed (320 r/min) and power (4.2 kW) of the wind turbine characteristics discussed in the previous section. The WRSG prototype from [24] (already available in the lab and, hence, a convenient test object), with a rated power of 4.2 kW was adopted for the direct-drive, medium-speed wind turbine system

investigated in this study. The prototype has non-overlapping, double-layer stator winding coils and a 16/18 pole/slot combination. The rated turbine speed from Figure 2 is used to determine the synchronous speed of this generator, which is 320 r/min at 43 Hz, putting it within the medium-speed range of 100 to 500 r/min. The cross-section layout of the finite element method (FEM) for the WRSG prototype is shown in Figure 3, and the specifications are listed in Table 1.

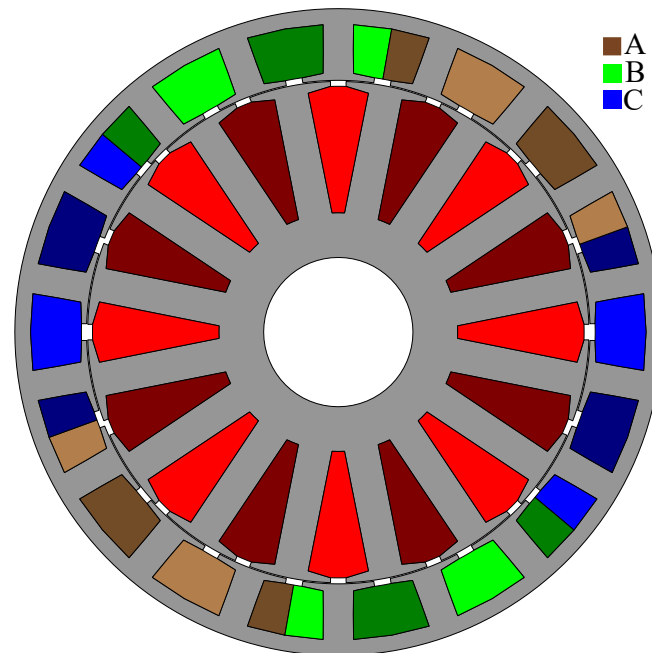


Figure 3. Two-dimensional model of the double-layer 16/18 pole/slot WRSG and coil arrangement, with light (positive) and dark (negative) colors.

Table 1. Specifications of the 16/18 WRSG.

Parameter	Value
Rated power	4.2 kW
Rated speed	320 r/min
Rated frequency	42.7 Hz
Rated torque	126.5 Nm
Stator outer diameter	260 mm
Rotor outer diameter	203.6 mm
Rotor inner diameter	60 mm
Stack length	125 mm
Air gap	0.45 mm
Stator turns per coil	67
Rotor turns per coil	150

3.2. Minimizing the Torque Ripple for WRSG

The 4.2 kW WRSG used in this study had an unfavorable torque ripple of 15.5%, which is not acceptable for small-scale wind turbines. There are various techniques to reduce torque ripple, such as skewing, pole shifting, and adding auxiliary slots to the stator teeth [25]. However, if the generator's torque ripple is very sensitive to manufacturing tolerances, then using any of the aforementioned methods might drastically affect the machine's performance and complicate the manufacturing process. The WRSG rotor used in this study was optimized to reduce the torque ripple using a precise but computationally less expensive coordinate descent method [26]. The coordinate descent technique, which is basically the first step in Powell's non-gradient method [27], is discussed and implemented in [26] to minimize the cogging torque of two PM wind generators for small-scale wind

energy systems. In this study, the stator of [24] was kept the same, but the rotor was optimized to minimize the torque ripple, and the optimal rotor was manufactured.

The coordinated descent approach optimizes the design for minimum torque output ripple by using a single parameter variation across all relevant dimensions. The relevant rotor dimensions that affect the torque ripple of the WRSG are

$$X = [rBs0 \quad rHs0 \quad rHs1]^T, \quad (4)$$

where $rBs0$ (rotor slot opening), $rHs0$ (rotor slot shoe 0), and $rHs1$ (rotor slot shoe 1) represent optimized rotor slot dimensions. These optimized dimensions are shown in Figure 4. Table 2 compares the optimized dimensions and the torque ripple of the WRSG after two iterations. The torque ripple versus mechanical rotor position waveforms for the base and optimized rotor WRSG using the coordinated descent method are shown in Figure 5. As shown in Table 2, the torque ripple is reduced from 11.5% to 7.77%, with the same turbine power.

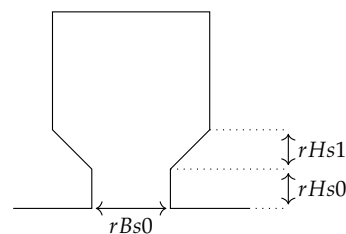


Figure 4. Optimized rotor slot dimensions of WRSG to minimize the torque ripple.

Table 2. Comparison between the optimized and base WRSG for minimizing the torque ripple.

Parameter	Base WRSG	Optimized WRSG
$rBs0$ (mm)	6.25	3.43
$rHs0$ (mm)	2.00	0.51
$rHs1$ (mm)	2.00	1.55
Torque ripple (%)	15.5	7.77

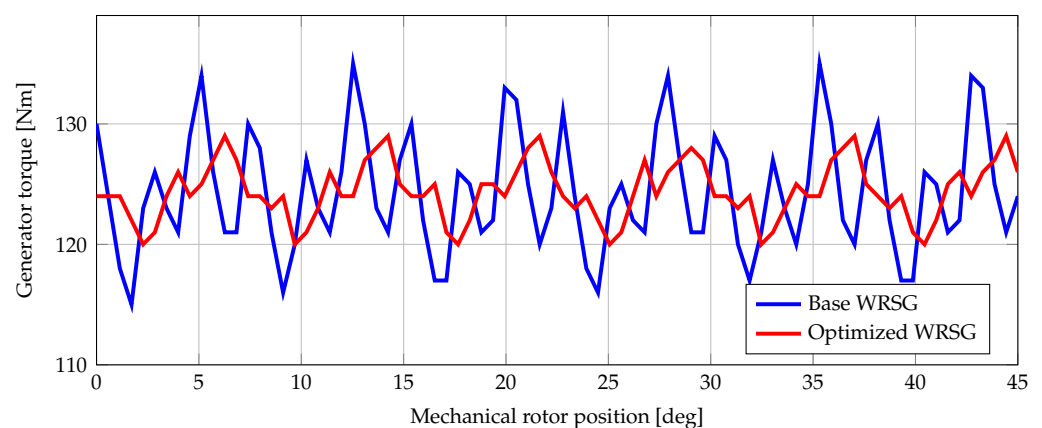


Figure 5. Generator torque versus mechanical rotor position for base- and rotor-optimized WRSG.

4. WRSG Modeling and Parameters

The dynamic modeling of the WRSG is described in this section. This section also shows how the WRSG parameters were determined using static finite element analysis (FEA) and the frozen permeability (FP) method.

4.1. Dynamic Model of WRSG

The dynamic WRSG model in the synchronous reference frame without damper windings (in order to simplify the model) is described in the generator operation (positive current out) as [28]

$$v_d = -R_s i_d + \frac{d\lambda_d}{dt} - \omega_e \lambda_q, \quad (5)$$

$$v_q = -R_s i_q + \frac{d\lambda_q}{dt} + \omega_e \lambda_d, \quad (6)$$

$$v_f = R_f i_f + \frac{d\lambda_f}{dt}, \quad (7)$$

$$\lambda_d = -L_d i_d + L_{df} i_f, \quad (8)$$

$$\lambda_q = -L_q i_q, \quad (9)$$

$$\lambda_f = \frac{3}{2} L_{df} i_d + L_{ff} i_f, \quad (10)$$

$$T_g = \frac{3}{4} p (\lambda_d i_q - \lambda_q i_d), \quad (11)$$

$$P_s = \frac{3}{2} (v_d i_d + v_q i_q), \quad (12)$$

where $v_{d,q}$ are the dq -axis stator voltages, v_f is the excitation voltage, $i_{d,q}$ are the dq -axis stator currents, i_f is the excitation current, R_s is the stator resistance, and R_f is the rotor resistance. The quantities $L_{d,q}$ are the dq -axis stator inductances, L_{ff} is the field-winding self-inductance, and L_{df} is the d -axis-to-rotor mutual inductance. $\lambda_{d,q}$ are the dq -axis stator flux linkages and λ_f is the field flux linkage. p is the number of poles and $\omega_e = \frac{p}{2} \omega_g$ is the rotor's electrical angular speed. The generator electromagnetic torque is T_g and P_s is the dq -axis stator power.

4.2. Generator Parameters Using Frozen Permeabilities

The WRSG achieves its maximum torque and efficiency over its entire range of operating points when the d -axis current is set to zero and only the field current and q -axis current are active. Therefore, the d -axis inductance of the stator will always be infinite when using (8). In this particular study, the FP method was used to calculate the value of this parameter so that it could be used in the Matlab/Simulink simulations. On a wound rotor synchronous machine, the FP technique was implemented for the first time in [29]. In today's modern world, the FP technique is widely recognized for its use in the methods of designing and controlling electrical machines [30,31].

In this study, the FP approach was implemented in the following steps:

1. A static non-linear FEA solution of the WRSG was simulated at the rated speed and current vector $[i_d, i_q, i_f]^T$. From this solution, the non-linear permeabilities of the WRSG were calculated.
2. The FEA permeabilities of all the WRSG mesh elements from the first step above were saved and frozen.
3. With these frozen permeabilities from step 2, three linear static solutions were simulated to determine the inductance parameters, L_d , L_q , L_{df} , and L_{ff} , based on (8) to (10). The three linear static FEA solutions are defined as follows:

$$L_d = \left. \frac{\lambda_d}{i_d} \right|_{i_f=i_q=0} \quad (13)$$

$$L_q = \frac{\lambda_q}{i_q} \Big|_{i_f=i_d=0'} \tag{14}$$

$$L_{df} = \frac{\lambda_d}{i_f} \Big|_{i_d=i_q=0'} \quad \text{and} \quad L_{ff} = \frac{\lambda_f}{i_f} \Big|_{i_d=i_q=0'} \tag{15}$$

The parameters determined using the FP method were then used to simulate the Matlab/Simulink model; they are shown in Table A1 along with the other parameters.

5. Wind Turbine System Control

Matlab/Simulink was used to evaluate the performance of the proposed MPPT current control for the WRSG-based wind turbine system. The overall control system that was developed is shown in Figure 6. It consists of the wind turbine model, which uses a look-up table to determine turbine torque based on wind speed and feedback of the turbine speed (Figure 7), two functions that determine the generator reference field current and q -axis current based on the turbine speed, a dq -axis current controller to output dq -axis voltages, a field current controller to output the field voltage, and lastly, the WRSG model in the synchronous reference frame.

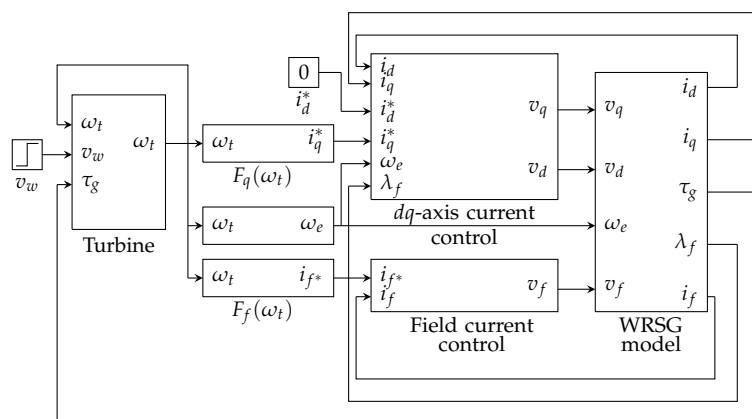


Figure 6. Matlab/Simulink block diagram of a variable-speed WRSG-based wind turbine system.

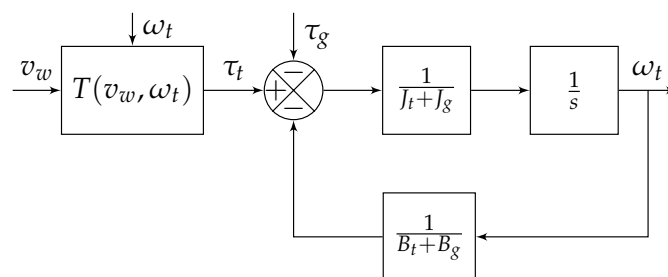


Figure 7. Matlab/Simulink diagram modeling the turbine dynamics.

5.1. Turbine Control

The Matlab/Simulink turbine control is shown in Figure 7. The dynamic model of the wind turbine is defined by

$$\tau_t - \tau_g = (J_t + J_g) \frac{d\omega_t}{dt} + (B_t + B_g)\omega_t, \tag{16}$$

where τ_t is the turbine’s electromechanical torque. ω_t is the turbine speed, which is equal to the generator speed, ω_g . J_t and J_g are the turbine and generator inertia, respectively. B_t and B_g are the turbine and generator viscous friction coefficients, respectively.

5.2. Generator MPPT Current Control

An offline method was adapted from the author’s previous work [32] in order to determine the optimal rotor field current and q -axis current while achieving MPPT with minimized copper losses by the WRSG. This unique method determines optimal WRSG currents as functions of the turbine speed based on steady-state FEA to achieve a second-degree polynomial fit of the MPP curve shown in Figure 2. Figure 8a,b show the optimal generator currents and the MPP curve as functions of generator speed, respectively. The generator currents are taken as reference currents, i_q^* (the command signal i_d^* is always kept at zero) and i_f^* , for the Matlab/Simulink simulations. The dq -axis current controller designed in Matlab/Simulink is shown in Figure 9a. Figure 9b shows the Matlab/Simulink field current controller design. The various current controllers use a classical PI regulator.

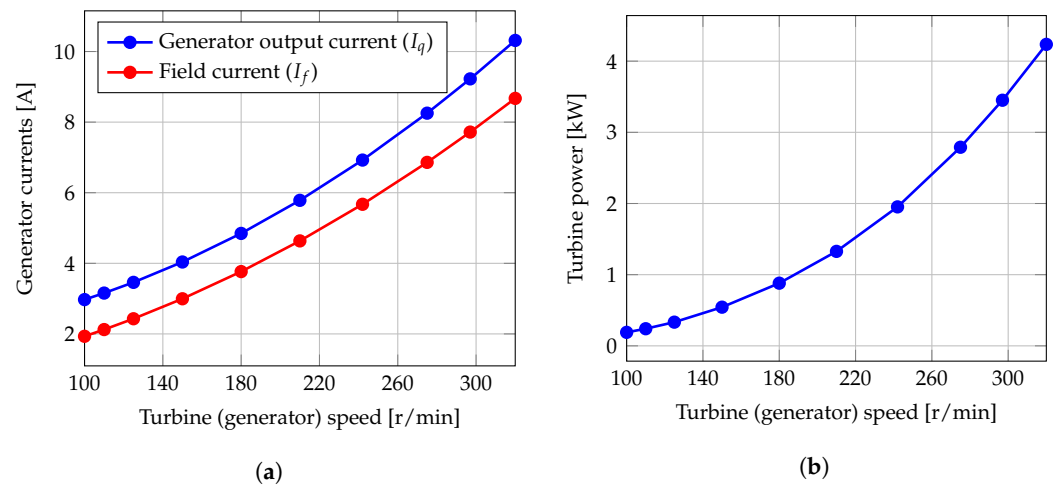


Figure 8. FEA (a) optimal generator output current (I_q) ($I_d = 0$) and rotor field current (I_f) for MPPT at minimized copper losses of the WRSG, and (b) turbine MPP curve as a function of the generator speed.

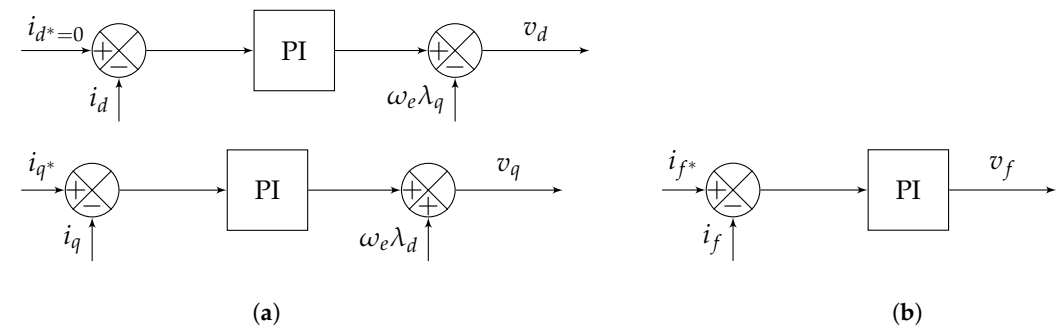


Figure 9. Matlab/Simulink diagram for (a) dq -axis current control and (b) field current control.

5.3. Transfer Function Derivation

To evaluate the robustness of the control system under dynamic conditions, the transfer function between the generator torque and turbine torque using Matlab/Simulink linearization functionality was found to be

$$\frac{\tau_g(s)}{\tau_t(s)} = \frac{963s^5 + 3 \times 10^6s^4 + 8 \times 10^8s^3 + 6 \times 10^{10}s^2 + 5 \times 10^{11}s + 4 \times 10^9}{s^7 + 6391s^6 + 10^7s^5 + 10^9s^4 + 10^{11}s^3 + 9 \times 10^{11}s^2 + 5 \times 10^{11}s + 4 \times 10^9}. \quad (17)$$

However, (17) can be represented by (18), which has the same characteristics as the original model of (17) but with minimal order, as shown in the Bode plot diagram in Figure 10a.

$$\frac{\tau_g(s)}{\tau_t(s)} \approx \frac{0.5726}{s + 0.5726}. \quad (18)$$

Figure 10a shows that the low-pass filter-transfer function of (17) has a -3 dB cut-off frequency of 0.1 Hz, which is very low. This implies that the system is stable, as all higher wind-speed frequencies are filtered out. To explain this low-pass filter characteristic, the mechanical transfer function between the turbine speed and turbine torque was obtained using the Matlab/Simulink linearization functionality:

$$\frac{\omega_t(s)}{\tau_t(s)} = \frac{0.05s^6 + 304s^5 + 5 \times 10^5s^4 + 5 \times 10^7s^3 + 5 \times 10^7s^2 + 4 \times 10^{10}s + 3 \times 10^8}{s^7 + 6391s^6 + 10^7s^5 + 10^9s^4 + 10^{11}s^3 + 9 \times 10^{11}s^2 + 5 \times 10^{11}s + 4 \times 10^9}. \quad (19)$$

Using the Matlab minimal realization functionality for pole-zero cancellation, (19) is reduced to a first-order dominant transfer function given by (20). The bode plot of (19) and (20) shown in Figure 10b verifies that the wind turbine acts as a low-pass filter with a -3 dB (because the DC sits at the -24 dB gain) cut-off frequency of 0.1 Hz, which is very low. This confirms that it is the large mechanical time constant of the wind turbine that is causing this low cut-off frequency.

$$\frac{\omega_t(s)}{\tau_t(s)} \approx \frac{0.04755}{s + 0.5726} \quad (20)$$

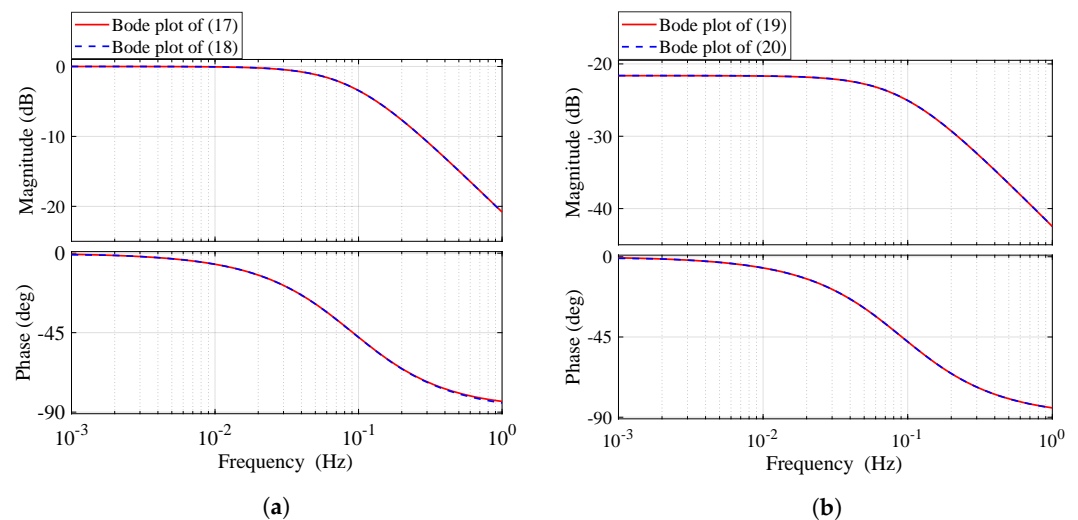


Figure 10. Bode plot of the transfer function for (a) the complete (mechanical and electrical) and (b) the mechanical part of the wind turbine system.

6. Simulation Results

This section presents the simulation results of the wind turbine system configuration presented in Figure 6. The system was tested using different wind speed profiles between and within the cut-in speed of 3 m/s and the rated speed of 12 m/s; the performance of the MPPT controller is analyzed in depth.

6.1. Step Change in the Wind Speed

The wind turbine system was subjected to a wind speed profile ranging from 3 m/s to 12 m/s and changing by 1 m/s every 100 s, as shown in Figure 11a. Figure 11b shows the turbine (generator) speed response. The maximum power point operation is shown in Figure 12, where Figure 12a shows the turbine power response and Figure 12b shows the turbine torque response. Figure 13a shows the actual and reference dq -axis current response,

while Figure 13b shows the actual and reference field current response. The results show that the MPPT current controller tracks the target current references.

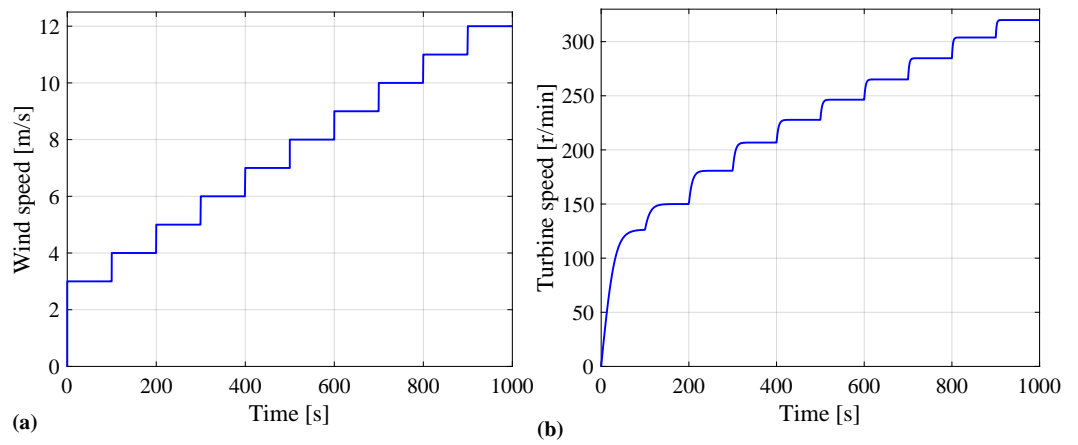


Figure 11. (a) Wind speed variation and (b) generator speed response versus time.

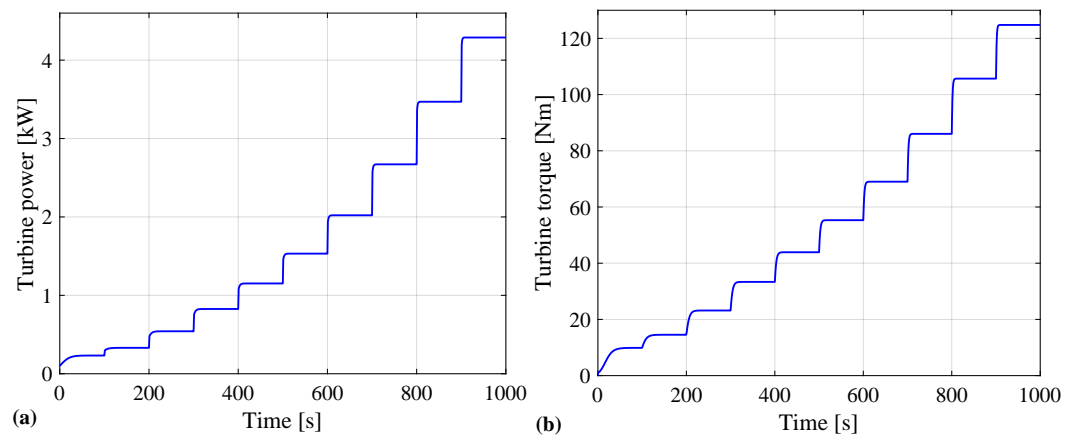


Figure 12. (a) Turbine speed and (b) turbine torque responses for wind speed variation versus time.

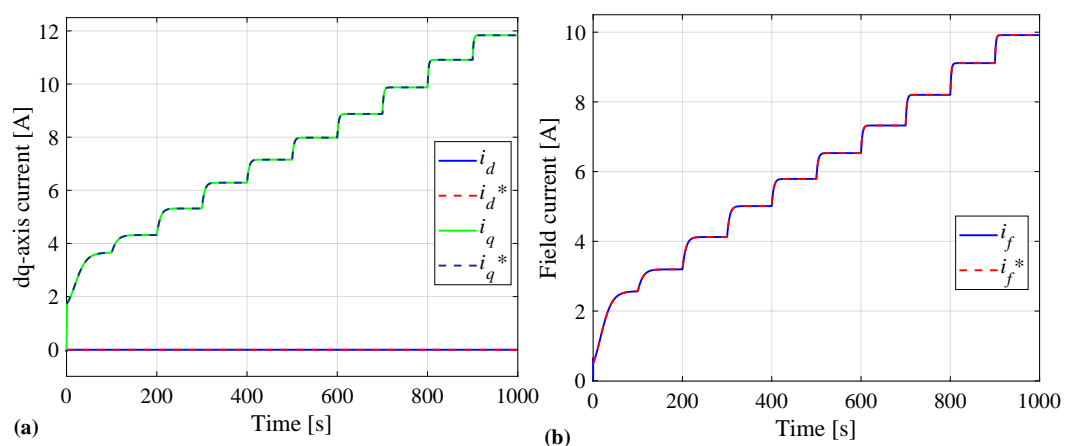


Figure 13. (a) dq -axis and (b) field current responses for wind speed variation versus time.

6.2. Wind Speed with a Frequency of 0.1 Hz

The wind turbine was subjected to a 0.1 Hz sinusoidal wind speed profile with an average speed of 10 m/s, as shown in Figure 14a. The turbine (generator) speed response is shown in Figure 14b. The actual and reference dq -axis current and field current responses are shown in Figure 15, and they track each other accurately.

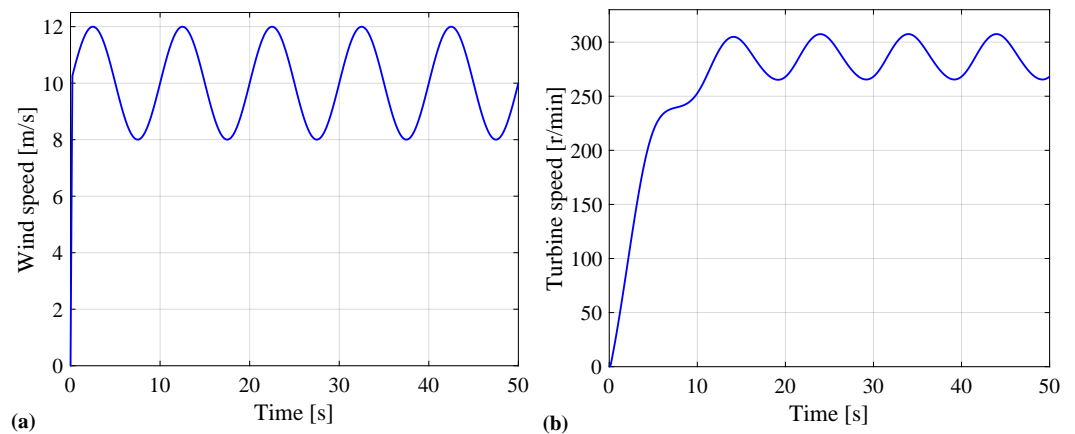


Figure 14. (a) Wind speed input of 0.1 Hz and (b) turbine speed response versus time.

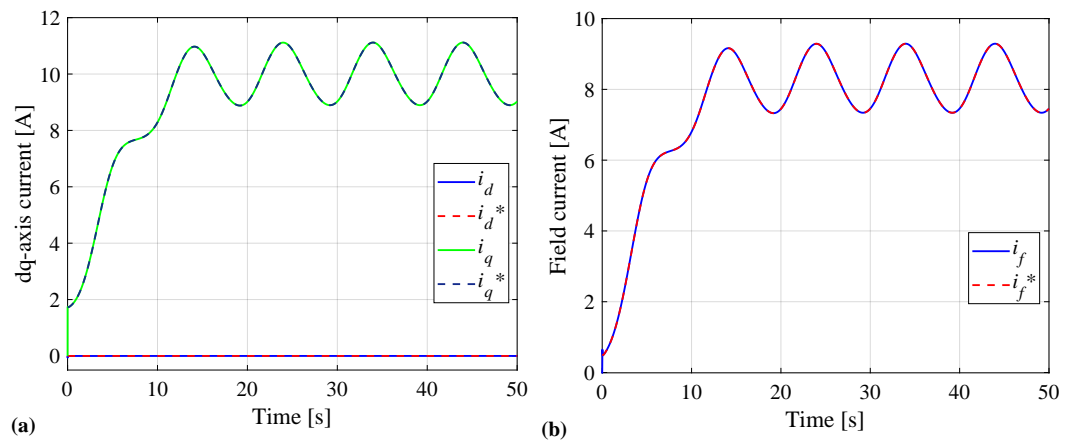


Figure 15. (a) dq -axis and (b) field currents for wind speed input of 0.1 Hz versus time.

6.2.1. Wind Speed with a Frequency of 1 Hz

The wind turbine was subjected to a 1 Hz sinusoidal wind speed profile with an average speed of 10 m/s, as shown in Figure 16a, and the low pass filter characteristic of the turbine system is seen in the turbine speed response shown in Figure 16b. The actual and reference dq -axis currents and field current responses are shown in Figure 17, and it can be seen that the actual and reference currents track each other accurately for a wind speed input of 1 Hz.

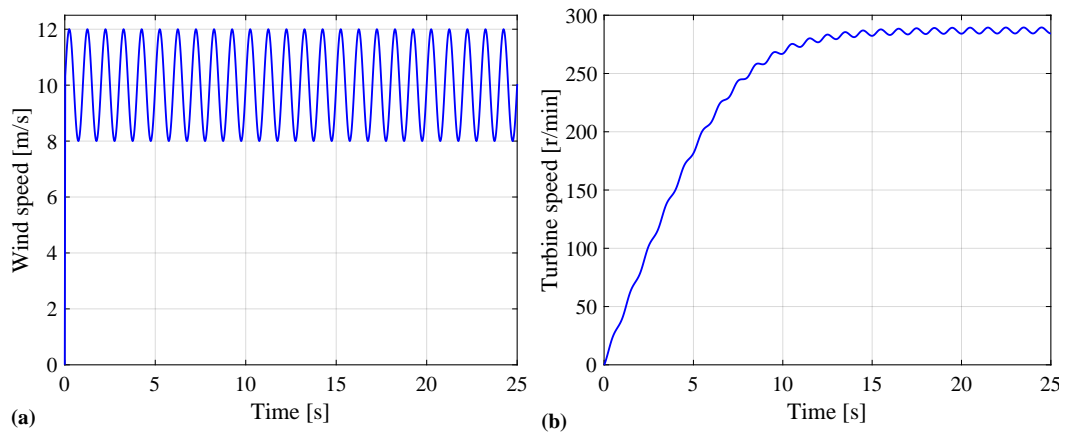


Figure 16. (a) Wind speed input of 1 Hz and (b) turbine (generator) speed response versus time.

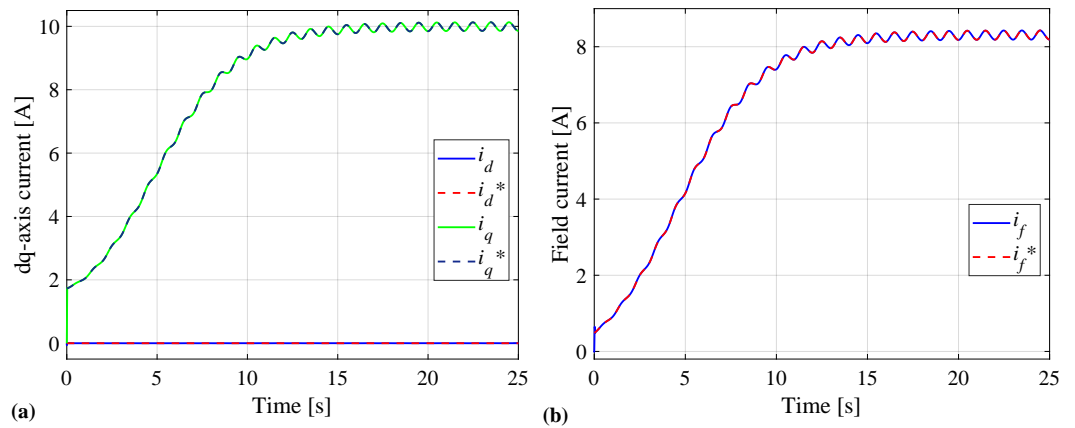


Figure 17. (a) *dq*-axis and (b) field currents for wind speed input of 1 Hz versus time.

6.2.2. Wind Speed with a Frequency of 10 Hz

A 10 Hz sinusoidal wind speed profile with an average speed of 10 m/s was applied to the wind turbine, as shown in Figure 18a. The turbine (generator) speed response is shown in Figure 18b. The actual and reference *dq*-axis current and field current responses are shown in Figure 19. It can be seen that the actual and reference currents track each other accurately for a wind speed input of 10 Hz.

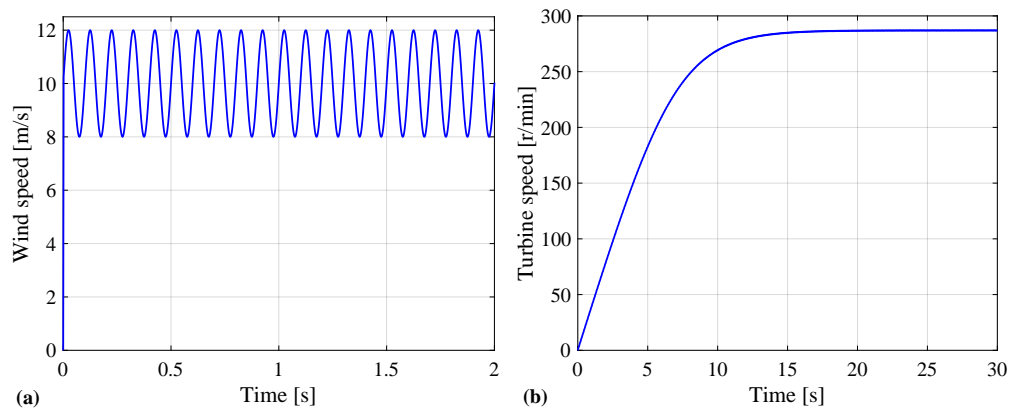


Figure 18. (a) Wind speed input of 10 Hz and (b) turbine (generator) speed response versus time.

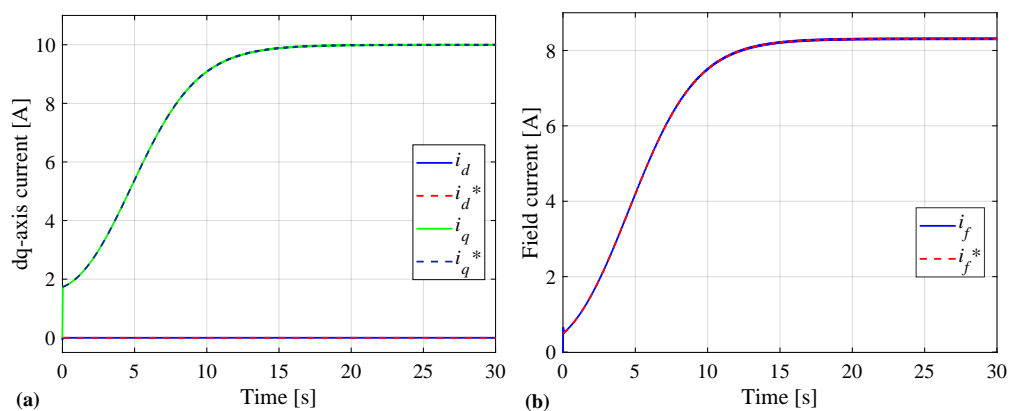


Figure 19. (a) *dq*-axis and (b) field currents for wind speed input of 10 Hz versus time.

7. Experimental Results

7.1. Experiment Setup

The experimental test bench setup is shown in Figure 20. A 22-kW four-pole induction machine (IM) coupled to a 1:2.6 reduction gearbox was used to emulate the wind turbine.

A flywheel was added to the IM to increase the mechanical inertia and emulate the wind turbine's inertia more accurately. A custom-built Pentium control system (Figure 21a) was used to control both the IM and WRSG through two back-to-back connected voltage source converters (VSCs). The input torque was measured using a USB torque sensor DR-3000 (Figure 21b) mounted between the IM and the WRSG. The torque sensor has a sensitivity of 0.1% and a rated torque range of 0.1 to 500 Nm. The rotor speed was measured using a 1024 pulse per revolution incremental encoder, which was connected to the Pentium control system through a digital-to-analog converter board. A 60 A/80 V DC power supply (Figure 21c) provided current to the field windings via brushes and slip rings.

The Pentium control system is built on Linux and includes an installed real-time application interface kernel module. It runs on a 1.5 GHz Pentium CPU that interfaces with a custom-built field programmable gate array (FPGA). This FPGA is in charge of sending control signals to the VSC boards. The VSC boards provide channels for measuring the currents of the IM and the WRSG, as well as the DC bus voltage. Because the VSCs are connected back to back, the Pentium control system, with its six pulse-width modulation output ports, can simultaneously control the IM and the WRSG. The VSCs used in this project were supplied by SEW-EURODRIVE, specifically for the Electrical Machines Laboratory at Stellenbosch University, and they are linked directly to the Pentium control system. They offer automatic current protection as well as appropriate dead-time switching. The resistors provide additional current protection in the event that the VSCs need to discharge energy through their breaking circuits.

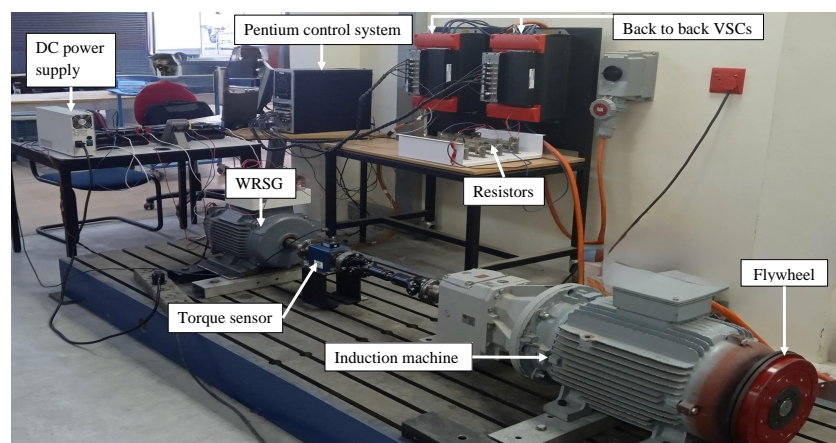


Figure 20. Practical system setup.

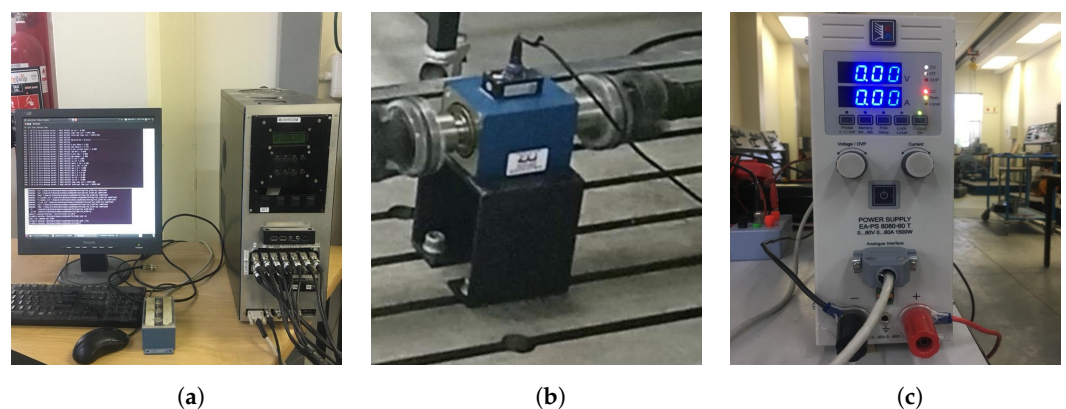


Figure 21. Photos of the (a) Pentium control system, (b) 80 V/60 A DC power supply, and (c) torque sensor.

7.2. WRSG Prototype

A new rotor was manufactured that was optimized using the coordinate descent method to reduce the torque ripple of [24]. The stack assembly and winding of this rotor

are depicted in Figure 22a,b, respectively. The manufactured stator was kept the same based on [24], and the complete winding within its frame is shown in Figure 22c.

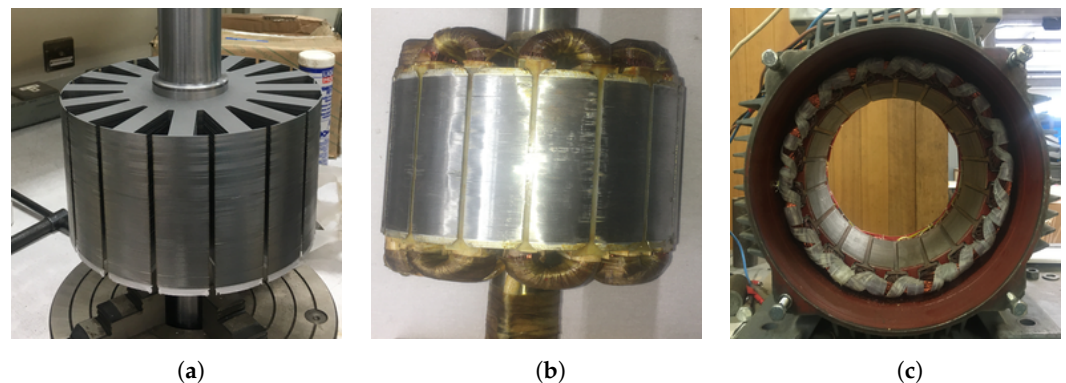


Figure 22. Photos of the manufactured prototype of the 4.2 kW 16/18 pole/slot WRSG. (a) Optimized rotor stack assembly, (b) optimized rotor winding, and (c) complete stator winding in its frame.

7.3. Steady-State Performance

The experimental steady-state results for the proposed wind generation system, as a function of turbine (generator) speed, are shown in Figure 23. The generator speed was estimated by a shaft encoder, and this value was used to determine the generator's current references, i_q ($i_d = 0$), and i_f . A signal from the Pentium control system was used to control the field current via remote control of the DC power supply. The field and q -axis currents are suitably controlled, as shown in Figure 23a, and have the same function as the optimal current references shown in Figure 7. The resulting turbine power versus generator speed tested with the MPPT generator currents is shown in Figure 23b; it can be seen that the FEA-predicted and -measured turbine power follow each other relatively well. Figure 23c shows the input (turbine) power and the generator output power versus the generator speed, and the efficiency performance is shown in Figure 23d. The generator efficiency from the mechanical input power to electrical output power varies from 95% to 75% at low speeds (100 to 220 r/min), which is effective for wind power generation because wind turbines operate in this region for more than 80% of the year.

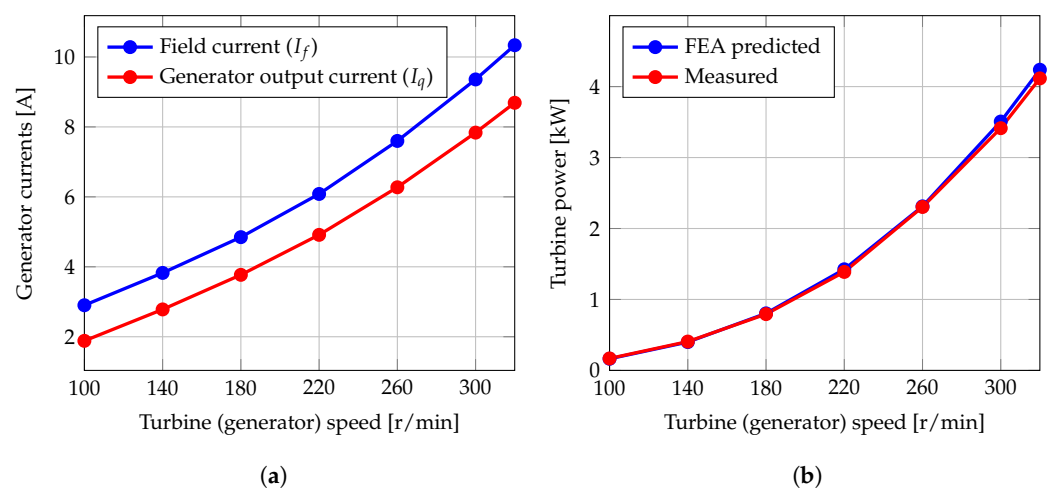


Figure 23. Cont.

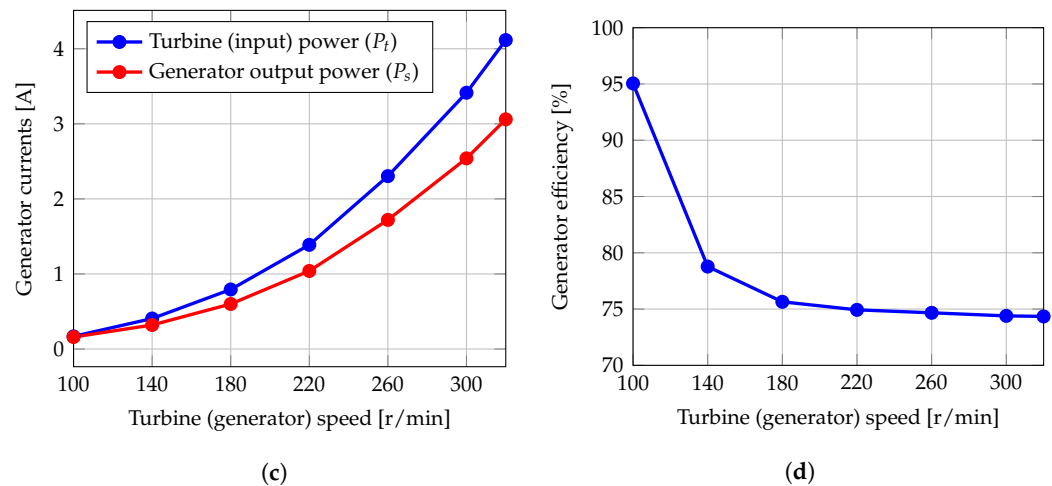


Figure 23. Experimental steady-state performance of the proposed MPPT wind generator current control as a function of speed. (a) Generator output current (I_q) ($I_d = 0$) and field current, (b) FEA-predicted and -measured MPP turbine power, (c) mechanical turbine input power, P_m and electrical generator stator output power, P_s , and (d) efficiency.

7.4. Dynamic Performance

An important aspect of any wind energy system, including the proposed system, is its stability under dynamic conditions. The experimental dynamic results for the proposed wind generation system are shown in Figures 24 and 25. The results in Figure 24 are for when the turbine speed is changing from 100 r/min to 320 r/min in steps of 20 r/min, and depict the turbine speed and power responses in Figure 24a,b, respectively.

The results shown in Figure 25 illustrate the behavior of the system when the turbine speed changes from 100 r/min to 320 r/min and back to 100 r/min. The turbine speed and power responses are depicted in Figures 24a,b, respectively. Figure 25a,b show the generator phase current and generator field current responses, respectively. These results, shown in Figures 24 and 25, demonstrate the effectiveness of the MPPT current-control method under dynamic conditions, highlighting the stability of the transition between different generator speeds, and hence wind speeds. The results also demonstrate the effectiveness of using simple speed functions to determine the optimal WRSG currents to achieve MPPT.

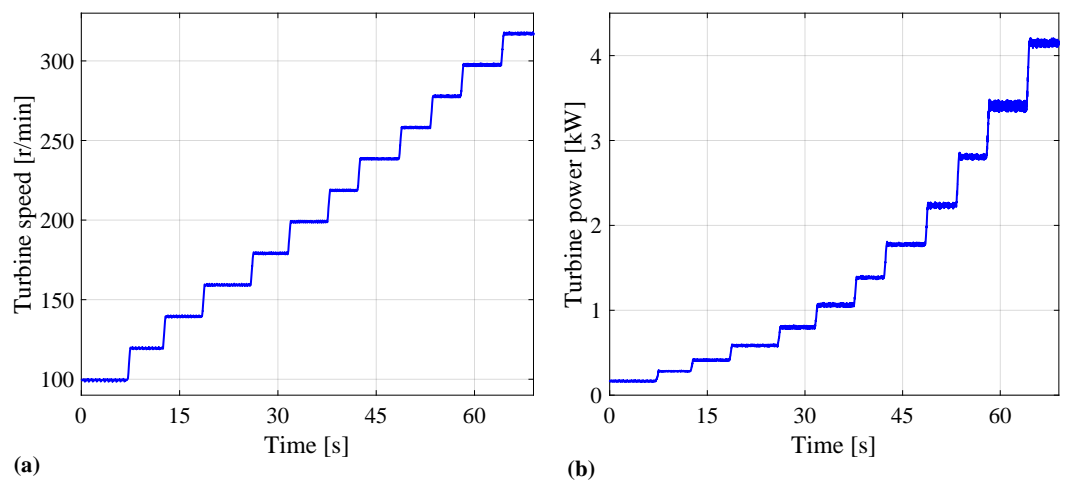


Figure 24. Measured (a) various turbine speeds and (b) turbine power responses versus time.

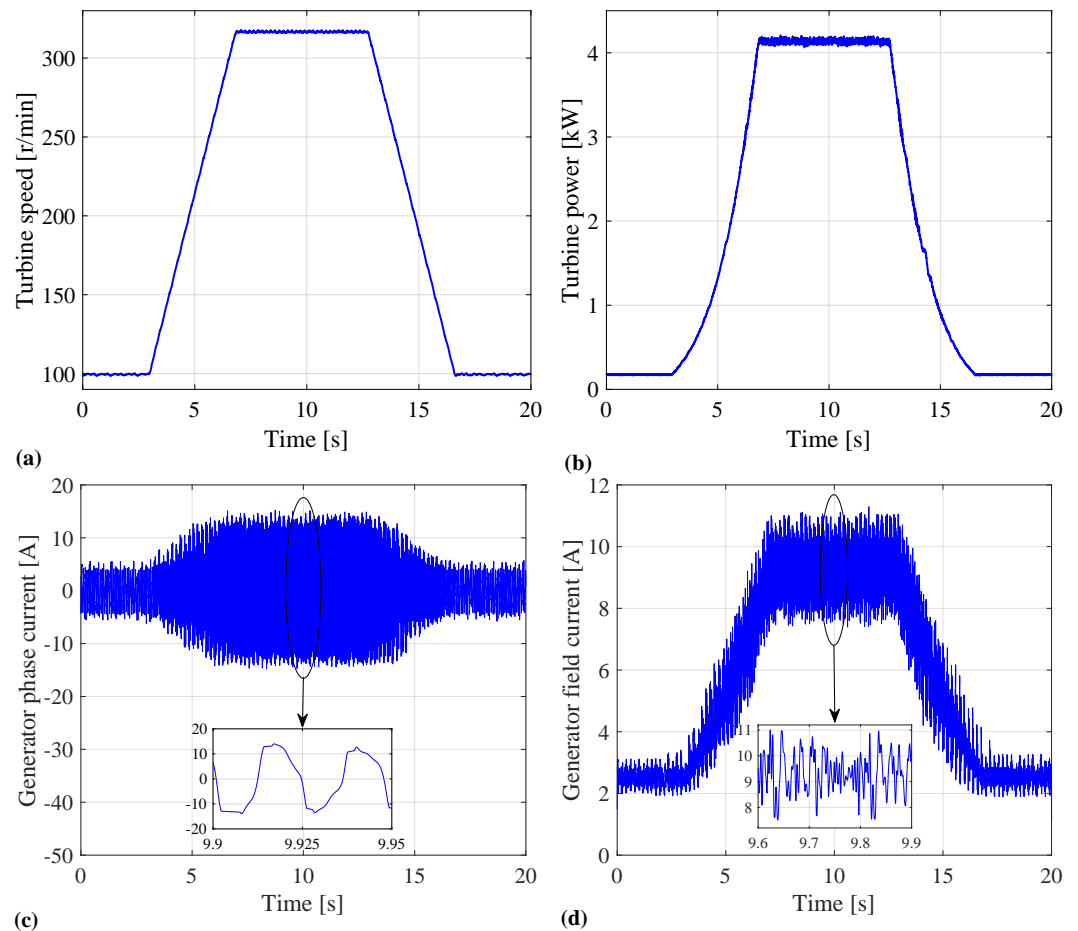


Figure 25. Measured step responses (a) turbine speed, (b) turbine power, (c) generator phase current, and (d) generator field current versus time.

7.5. Speed Profile with Different Frequencies

In this section, in order to further evaluate the robustness of the proposed MPPT current-control wind generation system, the performance of the system for speed references with different frequencies is presented. The different speed profiles, with average speed references of 260 r/min at 0.1 Hz, 1 Hz, and 10 Hz, are shown in Figures 26a, 27a and 28a, respectively. The turbine power responses for the speed profiles at 0.1 Hz, 1 Hz, and 10 Hz are shown in Figures 26b, 27b and 28b, respectively. Figure 27 shows that it is still following at 1 Hz. The reason for this is that the cut-off frequency of the practical lab system is much higher than that of the real system (the inertia is not as high). Figure 28 shows that, at 10 Hz, the system acts as a low-pass filter. However such high frequencies do not occur in real life. These measured results support the simulation results. They show that the system is stable and works well when the wind speed changes at different frequencies. They also show that the system acts as a low-pass filter at a high wind-speed frequency.

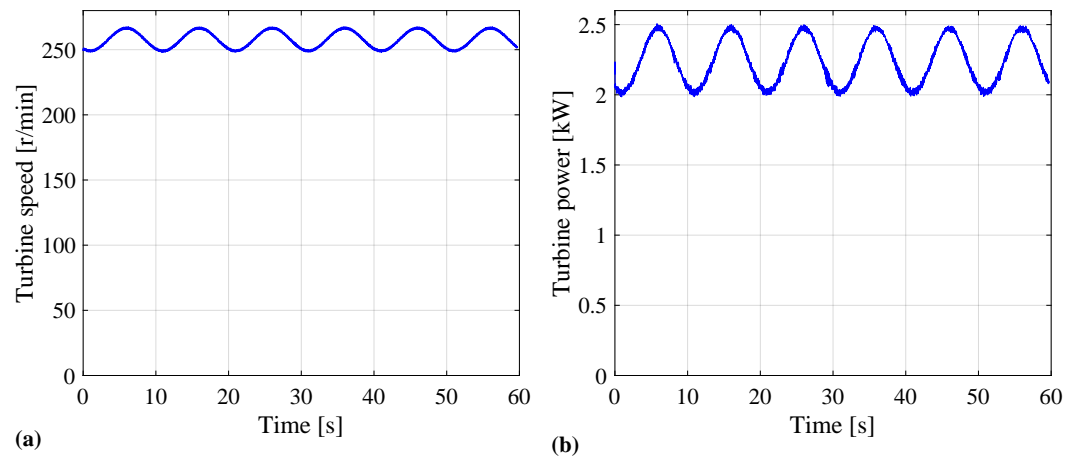


Figure 26. Measured (a) turbine speed with a frequency of 0.1 Hz and (b) the turbine power response.

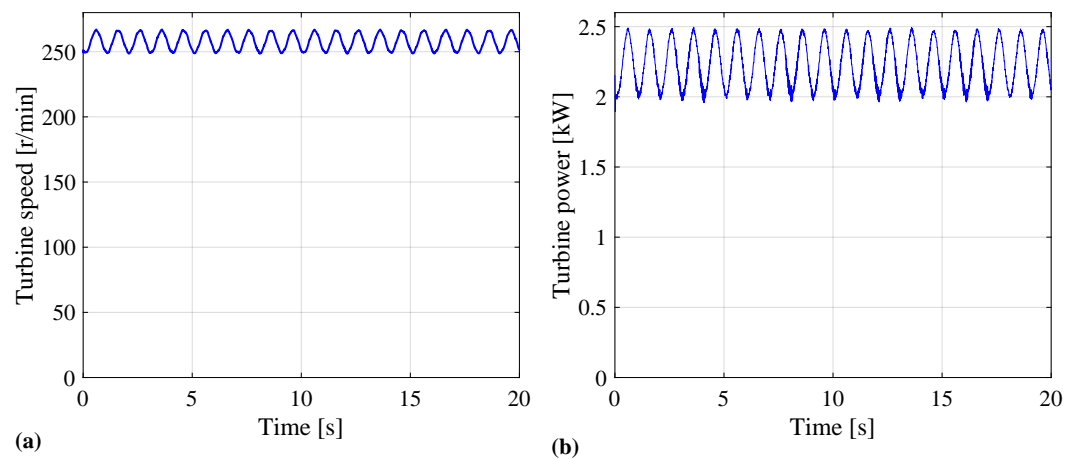


Figure 27. Measured (a) turbine speed with a frequency of 1 Hz and (b) the turbine power response.

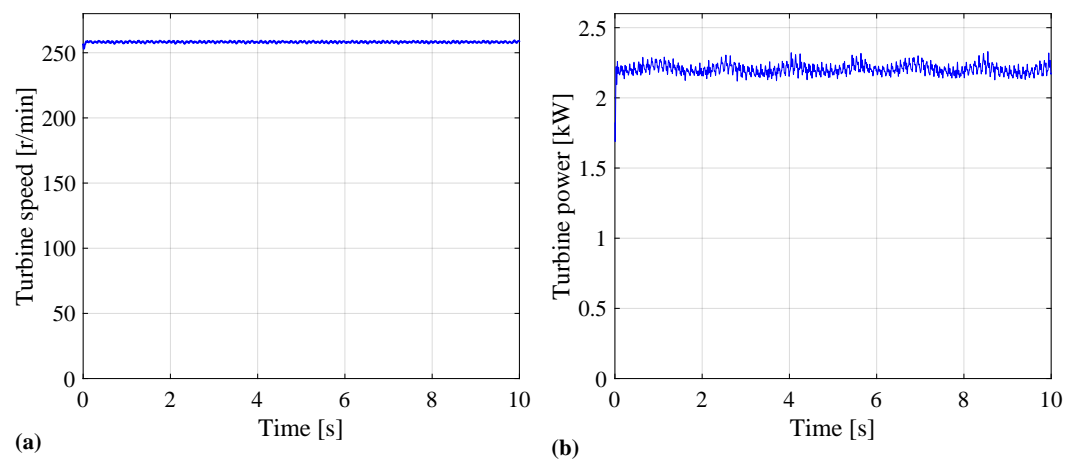


Figure 28. Measured (a) turbine speed with a frequency of 10 Hz and (b) the turbine power response.

8. Conclusions

In this study, a simple and robust MPPT current-control method for WRSG-based wind generation systems was investigated. Two simple turbine speed functions were used to determine the q -axis current (the d -axis current was always set to zero) and field current reference values to achieve MPPT of a WRSG-based wind turbine system. The simplicity of this method sets it apart from classical perturb and proportional-integral-derivative (PID) MPPT control methods.

The Matlab/Simulink simulation results under variable wind speeds demonstrate the robustness and effectiveness of the proposed MPPT current-control method for WRSG-based wind generation systems. The results obtained by choosing a sinusoidal-oscillating wind speed profile with three different frequencies demonstrate that the wind turbine system is stable and acts as a low-pass filter, mainly due to the large mechanical time constant of the wind turbine.

The proposed MPPT current-control method for WRSG-based wind turbines is validated by the experimental results. The experimental setup used a Pentium control system that was built in-house to demonstrate the system's simplicity and robustness by determining the MPPT generator's field and q -axis current references using two simple speed functions. In addition, the experimental results demonstrate that the proposed MPPT current-controlled wind energy system is robust against variations in wind speed and acts as a classical low-pass filter.

Author Contributions: Conceptualisation, L.D. and M.J.K.; methodology, L.D. and M.J.K.; software, L.D.; validation, L.D., M.J.K. and G.C.G.; formal analysis, L.D. and M.J.K.; investigation, L.D., M.J.K. and G.C.G.; writing—original draft preparation, L.D.; writing—review and editing, L.D., M.J.K., K.S.G. and G.C.G.; visualisation, L.D.; supervision, M.J.K. and K.S.G.; funding acquisition, M.J.K. All authors have read and agreed to the published version of the manuscript.

Funding: Centre for Renewable and Sustainable Energy Studies: Stellenbosch University, South Africa.

Data Availability Statement: The data for this study is presently archived with the first author, L.D., and can be made available.

Conflicts of Interest: The authors declare no conflict of interest.

Abbreviations

The following abbreviations are used in this manuscript:

CPU	Central Processing Unit
DC	Direct Current
DFIG	Doubly-Fed Induction Generator
DPC	Direct Power Control
EESG	Electrically Excited Synchronous Generator
FEA	Finite Element Analysis
FEM	Finite Element Method
FP	Frozen Permeability
FPGA	Field Programmable Gate Array
HCS	Hill Climb Search
IM	Induction Machine
INC	Incremental Conductance
IPC	Indirect Power Control
MPP	Maximum Power Point
MPPT	Maximum Power Point Tracking
OT	Optimal Torque
P&O	Perturb and Observe
PID	Proportional Integral Derivative
PI	Proportional Integral
PM	Permanent Magnet
PMSG	Permanent Magnet Synchronous Generator
PSF	Power Signal Feedback
RE	Rare Earth
RSG	Reluctance Synchronous Generator
SCIG	Squirrel Cage Induction Generator
SMC	Sliding Mode Control
TSR	Tip-Speed Ratio
VSC	Voltage Source Converter
WRSG	Wound Rotor Synchronous Generator

Appendix A

Table A1. Matlab/Simulink simulation parameters.

Wind Turbine	Value
Turbine inertia (J_t)	21 kg·m ²
Turbine friction (B_t)	0.007 N·m/s/rad
Wound rotor synchronous generator	
Stator resistance (R_s)	1.10 Ω
Rotor resistance (R_f)	2.63 Ω
d -axis inductance (L_d)	51.6 mH
q -axis inductance (L_q)	57.3 mH
Stator-to-rotor mutual inductance (L_{df})	88.4 mH
Field-winding self-inductance (L_{ff})	178 mH
Generator inertia (J_g)	0.002831 kg·m ²
Generator friction (B_g)	0.0001 N·m/s/rad
Pole pairs (p)	8
Rated power	4.20 kW
Rated torque	126.4 Nm
Rated speed	320 r/min
Cut-in speed	100 r/min

References

- Ritchie, H.; Roser, M.; Rosado, P. Energy. Our World in Data, 2022. Available online: <https://ourworldindata.org/energy> (accessed on 18 January 2023).
- Desalegn, B.; Gebeyehu, D.; Tamirat, B. Wind energy conversion technologies and engineering approaches to enhancing wind power generation: A review. *Heliyon* **2022**, *8*, e11263. [CrossRef] [PubMed]
- Dajaku, G.; Spas, S.; Gerling, D. Advanced optimization methods for fractional slot concentrated windings. *Electr. Eng.* **2019**, *101*, 103–120. [CrossRef]
- Zou, Y. Induction generator in wind power systems. In *Induction Motors-Applications, Control and Fault Diagnostics*; IntechOpen: London, UK, 2015.
- Roshanfekar, P.; Lundmark, S.; Thiringer, T.; Alatalo, M. A synchronous reluctance generator for a wind application-compared with an interior mounted permanent magnet synchronous generator. In Proceedings of the 7th IET International Conference on Power Electronics, Machines and Drives (PEMD 2014), Manchester, UK, 8–10 April 2014; pp. 1–5.
- Dmitrievskii, V.; Prakht, V.; Kazakbaev, V. Synchronous reluctance generator with ferrite magnets for wind turbine. *Proc. J. Physics Conf. Ser.* **2018**, *1102*, 012041. [CrossRef]
- Friedrich, G. Experimental comparison between wound rotor and permanent magnet synchronous machine for integrated starter generator applications. In Proceedings of the 2010 IEEE Energy Conversion Congress and Exposition, Atlanta, GA, USA, 12–16 September 2010; pp. 1731–1736.
- Ramadan, H.; Youssef, A.I.R.; Mousa, H.H.H.; Mohamed, E.E.M. An efficient variable-step P&O maximum power point tracking technique for grid-connected wind energy conversion system. *SN Appl. Sci.* **2019**, *1*, 1–15.
- Verma, N.; Banerjee, S.; Gupta, S.; Goyal, S.; Sharma, R. PMSG based WECS with MPPT via modified P&O algorithm. In Proceedings of the 2019 3rd International Conference on Recent Developments in Control, Automation & Power Engineering (RDCAPE), Noida, India, 10–11 October 2019; pp. 646–650.
- Kumar, M.B.H.; Saravanan, B.; Sanjeevikumar, P.; Blaabjerg, F. Review on control techniques and methodologies for maximum power extraction from wind energy systems. *IET Renew. Power Gener.* **2018**, *12*, 1609–1622. [CrossRef]
- Dursun, E.H.; Kulaksiz, A.A. Second-order sliding mode voltage-regulator for improving MPPT efficiency of PMSG-based WECS. *Int. J. Electr. Power Energy Syst.* **2020**, *121*, 106149. [CrossRef]
- Ganjefar, S.; Ghassemi, Ali A.; Ahmadi, M.M. Improving efficiency of two-type maximum power point tracking methods of tip-speed ratio and optimum torque in wind turbine system using a quantum neural network. *Energy* **2014**, *67*, 444–453. [CrossRef]
- Zebraoui, O.; Bouzi, M. Comparative study of different MPPT methods for wind energy conversion system. In Proceedings of the IOP Conference Series: Earth and Environmental Science, FST Fez, Morocco, 8–9 November 2017; Volume 161, p. 012023.
- Tiwari, R.; Babu, N.R. Fuzzy logic based MPPT for permanent magnet synchronous generator in wind energy conversion system. *IFAC-PapersOnLine* **2016**, *49*, 462–467. [CrossRef]
- Wang, Y.; Yu, Y.; Cao, S.; Zhang, X.; Gao, S. A review of applications of artificial intelligent algorithms in wind farms. *Artif. Intell. Rev.* **2020**, *53*, 3447–3500. [CrossRef]
- Morimoto, S.; Nakayama, H.; Sanada, M.; Takeda, Y. Sensorless output maximization control for variable-speed wind generation system using IPMSG. *IEEE Trans. Ind. Appl.* **2005**, *41*, 60–67. [CrossRef]

17. Soufyane, B.; Abdelhamid, R.; Smail, Z.; Elhafyani, M.L.; El Hajjaji, A. Fully Robust Sensorless Control of Direct-Drive PMSG Wind Turbine Feeding a Water Pumping System. *IFAC-PapersOnLine* **2020**, *53*, 12797–12802. [[CrossRef](#)]
18. Zheng, X.; Li, L.; Xu, D.; Platts, J. Sliding mode MPPT control of variable speed wind power system. In Proceedings of the 2009 Asia-Pacific Power and Energy Engineering Conference, Wuhan, China, 28–30 March 2009; pp. 1–4.
19. Avila, E.; Pozo, M.; Camacho, O.; Leica, P.; Ortega, L.; Gallardo, C.; Dominguez, X. Sliding-mode control in a cascade scheme for a PMSG based wind energy conversion system. In Proceedings of the 2017 IEEE Second Ecuador Technical Chapters Meeting (ETCM), Salinas, Ecuador, 16–20 October 2017; pp. 1–6.
20. Jingfeng, M.; Aihua, W.; Guoqing, W.; Xudong, Z. Maximum power point tracking in variable speed wind turbine system via optimal torque sliding mode control strategy. In Proceedings of the 2015 34th Chinese Control Conference (CCC), Hangzhou, China, 28–30 July 2015; pp. 7967–7971.
21. Bianchi, F.D.; Mantz, R.J.; De Battista, H. The wind and wind turbines. *Wind Turbine Control Systems: Principles, Modelling and Gain Scheduling Design*; Springer Science & Business Media: London, UK, 2007; pp. 7–28.
22. Masters, G.M. *Renewable and Efficient Electric Power Systems*; John Wiley & Sons: Hoboken, NJ, USA, 2013.
23. Chun, G.; Ganeshkumar, P.; Ahmed, A.; Park, J. Design of MPPT controller for small scale wind power system with PMSG. In Proceedings of the 2012 15th International Conference on Electrical Machines and Systems (ICEMS), Sapporo, Japan, 21–24 October 2012; pp. 1–4.
24. Kloppers, C.; Garner, K.S.; Kamper, M.J. Design and optimisation of a 16/18 wound rotor wind synchronous generator with non-overlap winding. In Proceedings of the 26th Southern African Universities Power and Engineering Conference, Johannesburg, South Africa, 24–26 January 2018.
25. Hwang, S.M.; Eom, J.B.; Jung, Y.H.; Lee, D.W.; Kang, B.S. Various design techniques to reduce cogging torque by controlling energy variation in permanent magnet motors. *IEEE Trans. Magn.* **2001**, *37*, 2806–2809. [[CrossRef](#)]
26. Labuschagne, C.; Kamper, M.J. Coordinate descent method to minimize cogging torque in small-scale wind generators. In Proceedings of the Southern African Sustainable Energy Conference, Stellenbosch, South Africa, 17–19 November 2021; pp. 182–187.
27. Powell, M.J. An efficient method for finding the minimum of a function of several variables without calculating derivatives. *Comput. J.* **1964**, *7*, 155–162. [[CrossRef](#)]
28. Fitzgerald, A.E.; Kingsley, C.; Umans, S.D. *Electric Machinery*, 6th ed.; McGraw Hill: New York, NY, USA, 2003.
29. Mabhula, M.; Kamper, M. Saliency and mutual inductance effect in cylindrical wound-rotor synchronous motor. In Proceedings of the 2017 IEEE Workshop on Electrical Machines Design, Control and Diagnosis (WEMDCD), Nottingham, UK, 20–21 April 2017; pp. 152–157.
30. Hittinger, C.; Hahn, I. Modeling of an IPMSM with short-circuited rotor winding for sensorless position estimation by FEA using the frozen permeability method. In Proceedings of the IECON 2017-43rd Annual Conference of the IEEE Industrial Electronics Society, Beijing, China, 29 October–1 November 2017; pp. 2067–2072.
31. Chen, J.; Li, J.; Qu, R.; Ge, M. Magnet-frozen-permeability FEA and DC-biased measurement for machine inductance: Application on a variable-flux PM machine. *IEEE Trans. Ind. Electron.* **2017**, *65*, 4599–4607.
32. Dube, L.; Garner, K.S.; Kamper, M.J. Multi three-phase converter-fed performance of non-overlapping winding wound rotor synchronous wind generator. In Proceedings of the 2022 International Conference on Electrical Machines (ICEM), Valencia, Spain, 5–8 September 2022.

Disclaimer/Publisher’s Note: The statements, opinions and data contained in all publications are solely those of the individual author(s) and contributor(s) and not of MDPI and/or the editor(s). MDPI and/or the editor(s) disclaim responsibility for any injury to people or property resulting from any ideas, methods, instructions or products referred to in the content.